# Electrochemical mechanism of ionic-liquid gating in antiferromagnetic Mott-insulating $NiS_2$ single crystals

Sajna Hameed,[1,*,†] Bryan Voigt,[2] John Dewey,[2] William Moore,[2] Damjan Pelc,[1] Bhaskar Das,[2] Sami El-Khatib,[3,2] Javier Garcia-Barriocanal,[4] Bing Luo,[4] Nick Seaton,[4] Guichuan Yu,[4,5] Chris Leighton,[2,‡] and Martin Greven[1,§]

[1]*School of Physics and Astronomy, University of Minnesota, Minneapolis, Minnesota 55455, USA*

[2]*Department of Chemical Engineering and Materials Science, University of Minnesota, Minneapolis, Minnesota 55455, USA*

[3]*Department of Physics, American University of Sharjah, Sharjah, United Arab Emirates*

[4]*Characterization Facility, University of Minnesota, Minneapolis, Minnesota 55455, USA*

[5]*Informatics Institute, University of Minnesota, Minneapolis, Minnesota 55455, USA*

(Received 28 December 2021; accepted 18 May 2022; published 7 June 2022)

We explore the effect of ionic-liquid gating in the antiferromagnetic Mott insulator $NiS_2$. Through temperature- and gate-voltage-dependent electronic transport measurements, a gating-induced three-dimensional metallic state is observed at positive gate bias on single-crystal surfaces. Based on transport, energy-dispersive x-ray spectroscopy, x-ray photoelectron spectroscopy, atomic force microscopy, and other techniques, we deduce an *electrochemical* gating mechanism involving a substantial decrease in the S:Ni ratio over hundreds of nanometers, which is both nonvolatile and irreversible. Such findings are in striking contrast to the reversible, volatile, two-dimensional *electrostatic* gate effect previously seen in pyrite $FeS_2$. We attribute this stark difference in electrochemical vs electrostatic gating response in $NiS_2$ and $FeS_2$ to the much larger S diffusion coefficient in $NiS_2$. The gating irreversibility, on the other hand, is associated with the lack of atmospheric S, in contrast to the better understood oxide case, where electrolysis of atmospheric $H_2O$ provides an O reservoir. The present study of $NiS_2$ thus provides insight into electrolyte gating mechanisms in functional materials, in a relatively unexplored limit.

DOI: 10.1103/PhysRevMaterials.6.064601

## I. INTRODUCTION

Chemical doping has long been a premier means to tune the charge-carrier density in insulators and semiconductors, providing access to vast regions of the phase diagrams of these materials [1]. The use of electric field to manipulate the carrier density in transistor-type structures provides an attractive alternative to chemical doping. The advantages of this approach include the potential to electrostatically dope charge carriers with minimal associated chemical disorder, as well as continuous and reversible tuning of the charge-carrier density. Conventional gate dielectrics such as $SiO_2$ enable the tuning of surface charge-carrier densities in transistors only up to $10^{13}$ cm$^{-2}$ before breakdown, however [2]. Electric-double-layer transistors (EDLTs) that employ an ionic liquid (IL) or ion gel as the gate dielectric have emerged as an attractive alternative and have enabled charge-carrier-density tuning to well in excess of $10^{14}$ cm$^{-2}$ [3–5]. This has triggered several breakthroughs, including the discovery of superconductivity in $KTaO_3$ [6], gate-induced superconductivity in $SrTiO_3$ [7,8] and the high-$T_c$ cuprates [4,9,10], control of the insulator-metal transition in $VO_2$ [11,12] and $NdNiO_3$ [13–15], gating-induced ferromagnetism in diamagnetic $FeS_2$ [16], and electrostatic modulation of ferromagnetism in $La_{1-x}Sr_xCoO_{3-\delta}$ [17].

In early investigations with electrolyte-based transistor devices, the charge-carrier induction was thought to be purely electrostatic in nature, resulting in reversible control of electronic properties. However, several studies, particularly of oxides, have shown that electrolyte gating can also proceed via electrochemical mechanisms, through the formation/annihilation of anion vacancies [3,8,12,18–23], $H^+$ introduction [24–27], etc. It must be emphasized that such electrochemical mechanisms are not necessarily less favorable than electrostatic ones, and that they can in fact be advantageous due to broader property modulation [3]. For instance, the electrochemical redox effect in $GdO_x$/Co/Pt devices, which induces migration of $O^{2-}$ ions towards/away from the Co layer upon application of an electric field, allows for nonvolatile voltage control of magnetism (which is advantageous due to low energy consumption [23]), and similar function can be achieved with electrochemical electrolyte gating. Quite generally, in order to achieve *predictive* control of materials via electrolyte gating, it is imperative to understand which properties of a material determine the extent of electrochemical vs electrostatic response. While progress along these lines has been made in oxides [21,28], information from other materials systems is clearly desirable.

The pyrite-structure first-row transition-metal disulfides ($TMS_2$) exhibit a wide variety of magnetic and electronic

*hamee007@umn.edu

†Present address: Max-Planck-Institute for Solid State Research, Heisenbergstraße 1, 70569 Stuttgart, Germany.

‡leighton@umn.edu

§greven@umn.edu

 

properties [29], including diamagnetic semiconduction ($FeS_2$ [16,30], $ZnS_2$ [31]), antiferromagnetic Mott insulation ($NiS_2$ [32–35]), antiferromagnetism with a rare spin-state crossover ($MnS_2$ [36,37]), ferromagnetic metallicity ($CoS_2$ [38]), and superconductivity ($CuS_2$ [29,31]). Recent work even reported the discovery of Weyl fermions in $CoS_2$ [39]. It is also possible to tune these materials via substitutional chemical doping to obtain interesting properties such as half-metallic (or at least highly spin polarized) ferromagnetism in $Co_{1-x}Fe_xS_2$ [38,40,41] and metamagnetism in $Co_{1-x}Ni_xS_2$ [42]. Importantly, the structure of this series of $TMS_2$ compounds is cubic $Pa\bar{3}$, and the electronic and magnetic properties are controlled by $d$-band filling. These compounds are thus potentially ideal for exploration of possible gate-induced magnetism, insulator-metal transitions, and superconductivity.

A recent investigation of the influence of IL gating on the diamagnetic semiconductor $FeS_2$ (electronic configuration $t_{2g}^6 e_g^0$) revealed a transition to a ferromagnetic metallic state at positive gate bias [16], constituting a demonstration of voltage-induced ferromagnetism from a diamagnetic state. Although semiconducting $FeS_2$ exhibits surface conduction that is extremely sensitive to surface structural and chemical modifications [43–46], the IL-gate-induced metallic state was observed to be strictly volatile and reversible (i.e., the initial semiconducting state was recovered after bias removal), providing strong evidence that the gating mechanism in this material is a simple electrostatic one [16]. In $NiS_2$, surface conduction was recently shown to be prominent as well, with extreme sensitivity to surface modification with, e.g., mechanical polishing [47]. We note that both the surface and the bulk in ungated pristine $FeS_2$ and $NiS_2$ are insulating in nature; the surface, however, is more conductive than the bulk, and hence shunts all transport current at low temperature, when the semiconducting bulk freezes out. Electronic transport in these materials in the pristine ungated state is thus effectively two-dimensional (2D) and insulating at low temperatures. This is also evident in prior surface-sensitive photoemission spectroscopy studies, which reveal a gaplike structure near the Fermi energy at low temperatures [48]. In terms of magnetism, $NiS_2$ adopts an antiferromagnetic Mott-insulating ground state with a Néel temperature of $T_N \approx 38$ K [33], and then undergoes a poorly understood first-order transition to a weak ferromagnetic state at $T_{wf} \approx 30$ K [33]. Prior work has shown that $NiS_2$ can be tuned to a metallic state with the application of pressure [49,50] or by substituting Se on the S site [50,51], but superconductivity has never been observed in doped $NiS_2$. In the phase diagram of the $TMS_2$ compounds, $NiS_2$ (electronic configuration $t_{2g}^6 e_g^2$) lies in close proximity to $CuS_2$ (electronic configuration $t_{2g}^6 e_g^3$), however, which exhibits superconductivity with a transition temperature of about 1.5 K [29,31]. $NiS_2$ is thus a fascinating candidate for possible gate-induced superconductivity, specifically at positive gate voltage, i.e., under electron accumulation.

Motivated by the above, here we study the effect of IL gating on single-crystal $NiS_2$. Through temperature- and gate-voltage-dependent electronic transport measurements, we observe a clear gate-induced metallic state at positive gate bias, with a progressively decreasing low-temperature sheet resistance with increasing gate voltage. Most surprisingly, and contrary to the highly reversible, volatile electrolyte-gate-induced surface insulator-metal transition in pyrite $FeS_2$ [16], transport, spectroscopy, and surface microscopy data on $NiS_2$ strongly support a nonvolatile, irreversible *electrochemical* mechanism involving a substantial voltage-induced reduction in the S:Ni ratio. Moreover, we find that this decrease in S:Ni ratio occurs over depths of hundreds of nanometers (nm), i.e., that the gate-induced metallic state is three-dimensional (3D) in nature, consistent with transport. We argue that this stark difference in gating mechanisms in $NiS_2$ and $FeS_2$ occurs due to the much larger S diffusion coefficient in $NiS_2$ [52] compared to $FeS_2$ [53,54]. This is analogous to the situation in electrolyte-gated oxides, wherein an electrostatic mechanism was established in materials such as $BaSnO_3$ due to low-room-temperature O vacancy diffusivity [28], in contrast to electrochemically responding materials such as $La_{1-x}Sr_xCoO_{3-\delta}$ with high O diffusivity [20–22]. No superconductivity is detected down to the lowest measured temperature of 450 mK in the gated $NiS_2$ system, possibly related to the strong inhomogeneity introduced by the gating. The irreversibility of the gating response in $NiS_2$ is likely associated with the absence of an atmospheric S reservoir in IL gating of sulfides; this is fundamentally different from oxide IL gating, where electrolysis of atmospheric $H_2O$ (present in ILs) serves as an essentially limitless O reservoir. These results thus provide substantial mechanistic understanding of electrolyte gating in a relatively unexplored limit.

## II. EXPERIMENTAL DETAILS

$NiS_2$ single crystals were grown via the chemical vapor transport method, as previously described [47]. Precursor powders of Ni (Alfa Aesar, 99.999% purity), S (CERAC, 99.9995% purity), and $NiBr_2$ (Sigma-Aldrich, 99.999% purity) were placed in sealed, evacuated ($\sim 10^{-6}$ Torr), quartz tubes. Crystal growth then proceeded for 13 days in a two-zone tube furnace with hot and cold zones at 700 °C and 650 °C. The hot and cold zones were briefly inverted at the start of the growth to clean the growth zone. Postgrowth, crystals were washed in solvent to remove residual S and $NiBr_2$. Extensive structural, chemical, magnetic, and electrical characterization of these crystals was reported previously [47].

Four-terminal resistance measurements were carried out in a van der Pauw configuration in a Quantum Design PPMS Dynacool system in the temperature range 1.8–300 K. The samples were contacted by Al wire bonding onto gold pads sputtered onto the sample surface. A Keithley 2612B sourcemeter was used in a four-terminal configuration to source the measurement current and measure the voltage. A separate Keithley 2400 sourcemeter was used in a two-terminal configuration to apply a gate voltage ($V_g$) with a concurrent measurement of the gate current ($I_g$). The gate voltage was applied at 300 K for 30 min, before cooling the sample to the base temperature. The IL used for gating was EMI-TFSI [1-ethyl-3-methylimidazolium bis(trifluoromethylsulfonyl) imide]. For low-temperature transport measurements to 0.45 K, we used a home-built $^3$He evaporation refrigerator with external gas handling. A high-throughput dipstick probe, directly inserted into the $^3$He pot, was used for these measurements. Unless otherwise stated, single crystals

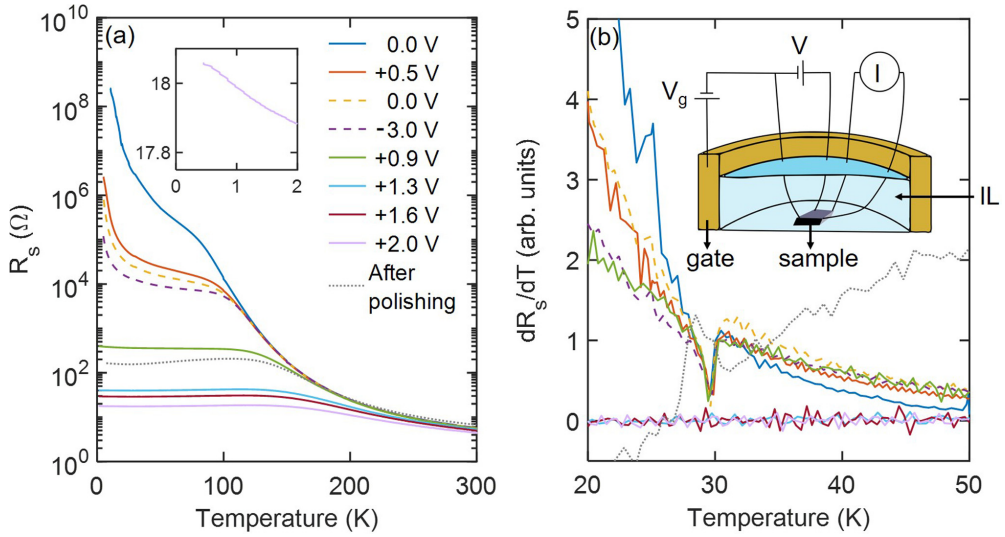


FIG. 1. (a) Sheet resistance as a function of temperature for different applied gate voltages. In the legend, the listing of applied voltages is in chronological order. As a check of the volatility and reversibility of the gate effect, 0 and −3.0 V (dashed lines) were applied following the first positive gate voltage application of +0.5 V. The resistance of the sample after polishing all sides postgating is also shown (dotted line). The inset shows low-temperature $R_s$ vs $T$ obtained for the +2.0 V gated sample in a $^3$He refrigerator. (b) Temperature derivative of the sheet resistances in (a), highlighting the anomaly at about 30 K due to the onset of weak ferromagnetism. The data are normalized to the value at a temperature slightly above 30 K (in the cases where an anomaly occurs). The anomaly disappears at an applied gate voltage of +1.3 V, but reappears after the gated surfaces are removed by mechanical polishing. Inset: schematic of the gating setup.

with a pristine (as-grown) top surface (on which the contacts were placed) and a mechanically polished bottom surface were used for all studies presented. This is important in light of the conclusions of our recent work on surface conduction [47], as discussed in more detail below.

Postgating characterization was performed after removing the IL from the crystal by sequential sonication in acetone and ethanol for about 30 min each. Chemical composition analysis was performed with a JEOL 6500 field-emission gun scanning electron microscope (FEGSEM) equipped with energy-dispersive x-ray spectrometry (EDX). Incident electron energies in the 5–20 keV range were used. X-ray photoelectron spectroscopy (XPS) measurements were carried out in a PHI 5000 VersaProbe III photoelectron spectrometer (ULVAC-PHI) with a monochromatic Al $K\alpha$ x-ray source. The base pressure of the system was $4 \times 10^{-10}$ Torr, and the pressure during data collection was $7.5 \times 10^{-9}$ Torr. A spot diameter of 100 $\mu$m was utilized. The C 1$s$ peak was used as a binding energy reference, with its energy set to 284.8 eV. Low-energy $Ar^+$ ion-gun and electron-gun neutralizers were used to mitigate surface charging of the samples. For depth profiling, a 3 kV $Ar^+$ ion gun with a sputter area of $3 \times 3$ mm$^2$ and a sputter rate of 4.3 nm/min (measured on $Si/SiO_x$) was used. Atomic force microscopy (AFM) was performed in contact mode on a Bruker Nanoscope V Multimode 8, and the data were analyzed using GWYDDION software [55,56].

## III. RESULTS AND ANALYSIS

A schematic of the EDLT geometry used to gate the $NiS_2$ single crystals is shown in the inset to Fig. 1(b). A gold-sputter-coated glass ring functions as both the gate electrode and as a container for the IL [16]. Single-crystal $NiS_2$ samples with pristine (as-grown) top surfaces and polished bottom surfaces were used for the measurements, with the electrical contacts applied on the pristine top surfaces. As described in detail in our recent work [47], the surface conduction in these $NiS_2$ crystals is very sensitive to the surface preparation. For simplicity, we focus here only on gating of pristine (i.e., as-grown, unpolished) surfaces. Figure 1(a) shows the temperature dependence of the sheet resistance ($R_s$) in a representative single-crystal $NiS_2$ EDLT at different applied $V_g$. At $V_g = 0$, typical semiconducting behavior is observed down to about 90 K, below which $R_s$ abruptly flattens, before increasing again at low $T$. This behavior arises from the aforementioned surface conduction in $NiS_2$ single crystals [34,47], where the more conductive surface shunts the insulating bulk at low $T$; this likely originates in surface states, which have been suggested to potentially be universal in $TMS_2$ compounds [47]. It must be noted that while the surface is more conducting than the bulk, it still remains insulating at low temperatures on pristine surfaces [47,48]. The transport in pristine $NiS_2$ single crystals is thus 2D and insulating at low temperatures.

Upon application of only $V_g = +0.5$ V, a drastic decrease in the low-$T$ sheet resistance (two orders of magnitude at 30 K) is observed. In order to probe the volatility and reversibility of this gate-induced resistance change, this was followed by returning to $V_g = 0$ V and then applying −3.0 V. As seen in Fig. 1(a), the observed gate effect is completely nonvolatile (compare the dashed yellow 0 V curve with the blue 0 V curve) and irreversible (compare the dashed purple −3.0 V curve with the blue 0 V curve). These observations essentially rule out a simple electrostatic gating mechanism (as observed in $FeS_2$ [16]), immediately implicating an

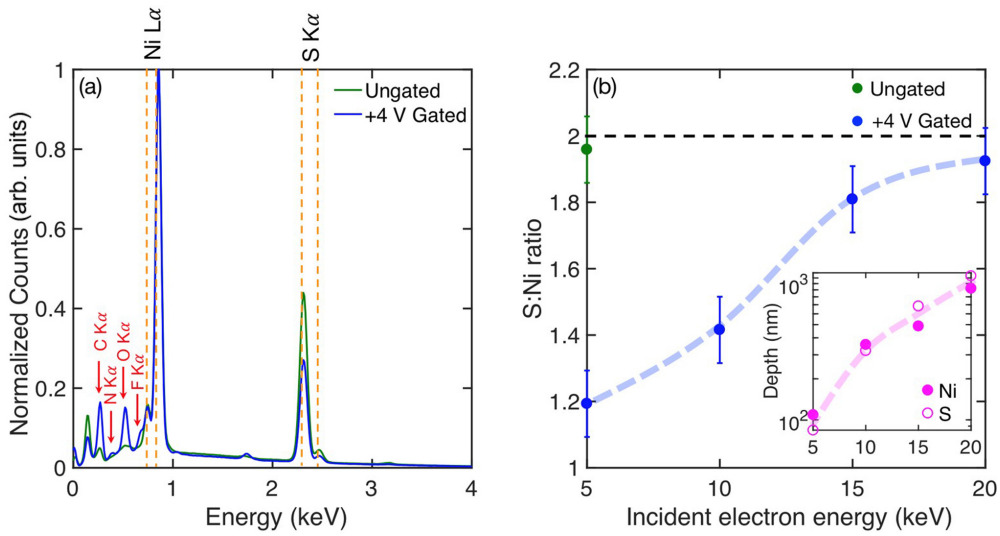


FIG. 2. (a) EDX analysis of a $NiS_2$ single crystal before and after gating (to +4.0 V). The spectra were obtained at an incident electron energy of 5 keV. The Ni and S peaks are marked by pairs of orange lines; common contaminant peaks are marked in red. The intensity is normalized to that of the most intense Ni peak. (b) S:Ni ratio obtained from EDX analysis of ungated and gated samples (+4.0 V) with different incident electron energies. The inset shows the depth below which 90% of the characteristic x rays are emitted from the sample for S and Ni, obtained from CASINO simulations (as discussed in the main text). The dashed lines in (b) are guides to the eye.

electrochemical mechanism, as we discuss extensively below. Further application of progressively more positive $V_g$ then results in even stronger decreases in low-$T$ resistance, with $R_s$ eventually falling far below the 2D quantum resistance (the inverse of the 2D minimum metallic conductance) of $\sim$26 k$\Omega$, to as low as $\sim$10 $\Omega$ at $V_g = +2.0$ V. Such very low absolute resistances, over 1000 times lower than the 26 k$\Omega$ threshold, imply that the electronic transport in the gated crystal is no longer 2D in nature, but instead very likely 3D. The derivative $dR_s/dT$ also becomes positive at this point, at least over some $T$ range, implying metallicity, along with the very low absolute $R_s$. Further gating to yet higher $V_g$ (up to +4 V) does not significantly change $R_s$ (see Supplemental Material, Sec. A [57]). We show below that these $R_s$ values far below 26 k$\Omega$ are in fact associated with strong reduction (i.e., an electrochemical gating mechanism), occurring over length scales of hundreds of nm into the crystal surface; the transition in Fig. 1(a) is thus definitively to a 3D metallic state. An attempt to recover the ungated state by polishing the sample surfaces postgating did indeed increase the low-$T$ resistance, but by barely an order of magnitude [see the dotted gray curve in Fig. 1(a)]. This is due to the fact that the surfaces of polished $NiS_2$ are substantially more conductive than pristine surfaces [47], rendering this approach unproductive. We did confirm that the dramatic decrease in sheet resistance with increasing positive gate bias also occurs in samples with initially polished gated surfaces, however (see Supplemental Material, Sec. B [57]). As a final comment on Fig. 1(a), note that these data were taken in a PPMS Dynacool system with a base temperature of 1.8 K. Additional transport experiments in a $^3$He refrigerator were performed on a crystal after gating to $V_g = +2.0$ V, but no superconductivity was detected down to 0.45 K [see the inset to Fig. 1(a)].

We also examined the temperature derivative of the sheet resistance, as shown in Fig. 1(b). A clear anomaly is observed at $T \approx 30$ K and $V_g = 0$ V, which is well known to be associated with the weak ferromagnetic transition in $NiS_2$ at $T_{wf} \approx 30$ K [47,52]. This anomaly persists to $V_g = +0.9$ V, but then completely disappears upon further gating to $V_g = +1.3$ V and above. This observation is highly significant, as the 30 K anomaly is known to be associated with $NiS_2$ specifically; it does not occur in lower-S-content Ni sulfides, such as NiS, $Ni_3S_4$, etc. Additionally, the anomaly is observed to reappear after polishing the sample surfaces postgating [see dotted curve in Fig. 1(b)]. Taken together with the observed nonvolatility and irreversibility of the gate effect [Fig. 1(a)], which strongly support an electrochemical (not electrostatic) mechanism, these observations clearly suggest substantial chemical changes to the $NiS_2$ surface with gate voltage, which we now explore with surface-sensitive chemical characterization techniques.

Figure 2(a) shows EDX spectra obtained from the top surface of a $NiS_2$ single crystal, both before gating, and after gating to $V_g = +4.0$ V and then removing the IL. Apart from the usual O and C signals due to surface contamination, the ungated sample shows only the expected Ni and S core transitions. In the gated sample, additional weak F (fluorine) and N (nitrogen) signals are visible, due to residual IL on the sample surface [20]. More importantly, the spectral intensities in Fig. 2(a) are normalized to those of the most intense Ni peak, the strong decrease in S intensity after gating therefore providing clear evidence of gating-induced reduction (i.e., a decrease in the S:Ni ratio) in these data acquired at 5 keV incoming electron energy.

In EDX, the energy of the incident electron beam determines the depth to which the electrons penetrate, the generation volume within which the emitted photons originate, and thus the effective probe depth. This is illustrated in the inset to Fig. 2(b), which shows the depth below which 90% of the x rays are ejected from the sample and detected,

for varying incident electron energies (from the 5–20 keV studied in our experiments). These probing depths were calculated using the Monte Carlo simulation of electron trajectories available in the CASINO software package [58]. As shown in Fig. 2(b), varying the incident electron energy thus enables depth profiling of the S:Ni ratio, from ∼100 to ∼1000 nm. At 20 keV, for example, where x rays are ejected from depths up to ∼1000 nm (inset), the gated $NiS_2$ crystal has a S:Ni ratio of $1.92 \pm 0.10$ (systematic error dominated), corresponding to stoichiometric $NiS_2$ within error. As also shown in Fig. 2(b), this is essentially identical to the ungated crystal (green point), consistent with our prior work [47]. With decreasing incident electron energy (and hence probing depth), however, a strong decrease in the S:Ni ratio is observed in the gated case [Fig. 2(b)], directly evidencing gate-induced reduction, with the effect being strongest at the surface. At 5 keV, for example [∼200 nm probing depth (inset)], the measured S:Ni ratio of $1.19 \pm 0.10$ is drastically reduced from that of stoichiometric $NiS_2$. Note that the same sample surface measured at 5 keV before gating shows a S:Ni ratio of $1.96 \pm 0.10$, leaving no doubt that the low S:Ni ratio measured on the gated surface is induced by gating, rather than some systematic EDX error. A reduction of the S:Ni ratio to values between 1.1 and 1.3 at 5 keV incident electron energy was observed in all (four) samples gated to $V_g \geqslant +2.0$ V (data not shown). As already deduced indirectly from transport measurements, the gating effect in these $NiS_2$ crystals thus clearly results from an electrochemical mechanism associated with reduction at positive $V_g$, and not from electrostatic surface doping of electrons. This electrochemical reduction apparently takes place over surprisingly large depths, of the order of hundreds of nm. This is unusual but not unprecedented in electrochemical-based electrolyte gating. In perovskite cobaltites, for example, reduction at positive gate voltage can take place over more than 100 nm, enabled by a high O diffusion coefficient at room temperature [21,22].

Examination of the Ni-S equilibrium phase diagram reveals that, with S reduction, the room-temperature-stable phases most likely to be induced with a S:Ni ratio between 2 and 1 are $Ni_3S_4$ (S : Ni = 1.33) and NiS (S : Ni = 1) [59]. Further decrease of the S:Ni ratio to values below 1 could potentially induce $Ni_9S_8$ and $Ni_3S_2$, although other metastable phases are also possible [59], as well as oxides and hydroxides, which we return to below. While our EDX results clearly establish strong reduction to S:Ni ratios of ∼1.2 near the crystal surfaces after gating, this technique provides no information regarding the specific phases present. To understand this further we thus also carried out XPS measurements, which enable the determination of binding energies, and hence changes in the valence state of specific elements. Such a change in valence would be expected, e.g., if conversion of $NiS_2$ to NiS occurs in the surface region during gating. In this specific case, both $NiS_2$ and NiS have Ni in the +2 valence state, with S valence states of $(S_2)^{2-}$ (i.e., $S^{1-}$) and $S^{2-}$, respectively. This specific scenario would thus induce a change in S valence, but not in Ni valence. On the other hand, reduction to $Ni_3S_4$ would generate $S^{2-}$ with mixed 2 + /3+ valence for Ni, a difference that ought to be distinguishable by XPS. Note here that the XPS probing depth is determined by the energy-dependent mean free path of the emitted photoelectrons, typically a few nm, rendering XPS far more surface sensitive than energy-dependent EDX.

Figures 3(a) and 3(b) show XPS survey scans of $NiS_2$ crystal surfaces before gating and after gating to $V_g = +4.0$ V, respectively. Various Ni and S spectral peaks are clearly discernible, in addition to expected contaminant peaks due to C and O. In Fig. 3(b), additional contaminant peaks from F and N are also visible, arising from residual IL [20]; stronger C and O contamination is also visible in (b), as might be expected. Figures 3(c) and 3(d) then show high-resolution scans around the S $2p$ and Ni $2p_{3/2}$ peaks, respectively. The data in these figures were taken before gating (dark green); after gating to +4.0 V, then removing the IL (blue curves immediately above the dark green curves); and additionally after $Ar^+$-ion sputtering of the gated surface to the sputtered thickness as indicated on the right side of the figures. These sputtered thicknesses are based on sputter rates that were calibrated on a $Si/SiO_x$ substrate and are thus approximate.

As shown in Fig. 3(c), the S $2p_{3/2}$ and $2p_{1/2}$ peaks in the ungated case (bottom curve) occur at 162.2 and 163.5 eV, respectively, in good agreement with prior work on $NiS_2$ [60] and $FeS_2$ [61]. After gating (blue curve immediately above the dark green curve), clear shifts of these S $2p$ peaks to lower binding energy occur, along with a decrease in signal-to-noise ratio due to the residual IL and associated surface damage. Importantly, this is exactly as expected for conversion from $S^{1-}$ to $S^{2-}$, and is in fact very similar to observations for NiS and $Fe_{1-x}S$ [60,61]. Note that an additional broad spectral component is observed in the postgating S high-resolution scan at ∼168 eV, very possibly arising from residual TFSI on the gated surface [62]. After $Ar^+$-ion sputtering ∼6 nm off the gated surface (red line), the S $2p$ peaks regain features *somewhat* reminiscent of the pristine $NiS_2$ surface, although they retain distinct differences, specifically broader widths, slight binding energy shifts, and lesser splitting. It must be emphasized at this point that the sputtering process itself can introduce surface damage, defects, and nonstoichiometry, which could influence the postsputtering XPS spectra in Fig. 3(c) [63]. We thus characterized the extent of such sputtering-induced chemical changes by performing XPS measurements on an ungated pristine sample as a function of sputtering time/depth (see Supplemental Material, Sec. C [57], Fig. S3). We find that, while the peak splitting, exact peak shapes, and intensity ratio of the S $2p_{3/2}$ and $2p_{1/2}$ peaks may be influenced by sputtering, the position of the S $2p_{3/2}$ peak remains largely unaffected, and therefore provides a robust probe of the S valence state. Measurement of the S $2p$ spectrum after further sputtering of postgating surfaces [Fig. 3(c)] reveals that the S $2p_{3/2}$ peak shifts back and forth between the position expected for the ungated phase and that expected for the S-reduced phase. This indicates depthwise inhomogeneity in the S:Ni ratio, evidence for overall reduction in the S:Ni ratio extending to over 400 nm depths in Fig. 3(c), consistent with our EDX analysis. In addition, *lateral* variability is also observed for the intensity of the broad ∼168 eV feature in the S $2p$ spectrum of the gated sample (Fig. S4 [57]). This is expected as residual ionic liquid would naturally be expected to be distributed inhomogeneously on the gated surface (as seen in prior microscopy work on other electrolyte-gated oxides [20]).

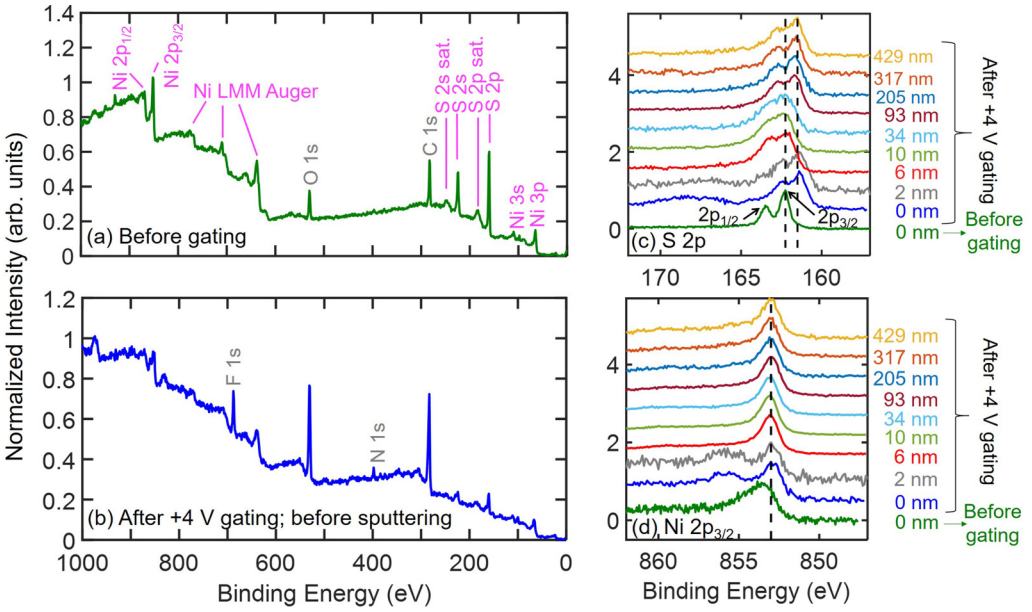


FIG. 3. XPS survey scans taken on the crystal surface (a) before gating (no IL applied) and (b) after gating (+4.0 V), but before argon-ion sputtering. The XPS peaks due to specific elements are marked in (a); in (b), only the peaks due to IL contamination are additionally marked. High-resolution XPS scans of the S $2p$ and Ni $2p_{3/2}$ peaks are shown in (c), (d), respectively. The bottom spectra in dark green and blue correspond to panels (a), (b), respectively. The rest of the spectra were obtained with argon-ion sputtering. The approximate thickness of material sputtered before the measurement of each spectrum is indicated. These sputter thicknesses are based on sputter rates that were calibrated on a $Si/SiO_x$ substrate and are thus approximate. Note that the spot at which the spectra were measured postsputtering (gray curve and all other curves above it) is different from the spot at which the spectrum was measured after gating, but before any sputtering (blue curve).

Despite the strong shifts seen for the S peaks in Fig. 3(c), the primary Ni $2p_{3/2}$ peak in Fig. 3(d) shows only a slight shift after gating, and this shift is observed to persist after sputtering. Note that no shift of the Ni $2p_{3/2}$ peak would be expected if the gating-induced phase were NiS, in which Ni remains in the same 2+ valence state as $NiS_2$. Such a shift was also observed in an ungated sample after sputtering (see Supplemental Material, Sec. C [57], Fig. S5), and is therefore inherent to the surface of pristine $NiS_2$ samples and does not result from gating. This could possibly be related to the surface states that are argued to be responsible for the surface conduction observed in pristine $NiS_2$ single crystals [47]. More significantly, a higher binding energy (∼856 eV) hump emerges after gating (blue line), which disappears after sputtering ∼6 nm off the gated surface (red line). Such a higher binding energy feature would be expected for $Ni_3S_4$, in which Ni has mixed $2+/3+$ valence [64]. Combining the conclusions from S and Ni XPS, it is thus likely that both NiS and $Ni_3S_4$ form under electrochemical reduction, consistent with the postgating surface S:Ni ratio from EDX of ∼1.2, which is intermediate between NiS and $Ni_3S_4$. The intensity of the higher binding energy feature is observed to change, depending on the position at which the spectrum is measured, which indicates lateral inhomogeneity (Fig. S4 [57]). We wish to stress here that both depthwise and lateral inhomogeneity, as clearly deduced from our XPS data (e.g., Fig. 3(c) and Fig. S4 [57]), are likely inevitable in electrochemical gating, meaning that coexistence of NiS and $Ni_3S_4$ is entirely reasonable. Other phases such as oxides and hydroxides of Ni are also possible, which would also be consistent with the presence of the higher binding energy feature in the Ni $2p_{3/2}$ spectrum [65,66]. Measurement of the Ni $2p_{3/2}$ spectrum after sputtering beyond ∼6 nm reveals no significant differences with the "ungated" Ni $2p_{3/2}$ spectrum, implicating that the oxidized-Ni phase is strongly surface localized. We note that a full depth-dependent analysis of XPS intensities was also attempted (see Supplemental Material, Sec. C [57], Fig. S6), to depths of ∼100 nm. Unfortunately, this was inconclusive with respect to the near-surface depth dependence of the S:Ni ratio, primarily due to strong effects of gating on the surface topography, as discussed below. As a final note on XPS, while depthwise and lateral inhomogeneity are evidenced, we emphasize that the gating effect on S $2p$ and Ni $2p_{3/2}$ XPS spectra observed here is highly reproducible, as emphasized in Supplemental Material, Sec. D [57].

Before moving to surface topography, we first comment on the correspondence of the above EDX and XPS results with the transport data in Fig. 1. The most important point here is that both NiS and $Ni_3S_4$ are known to support metallic conductivity. NiS exists in two forms: (i) hexagonal $\beta$-NiS exhibiting a transition to an antiferromagnetically ordered state below $T_N \approx 264$ K, accompanied by a metal-semiconductor or metal-metal transition [67,68]; and (ii) rhombohedral $\gamma$-NiS exhibiting metallic conductivity [68]. Off-stoichiometric $\beta$-NiS and sintered $\gamma$-NiS also exhibit metallic conductivity, with low-$T$ resistivities that have been reported to reach as low as ∼1 $\mu\Omega$ cm [69,70]. $Ni_3S_4$, on the other hand, exhibits ferrimagnetism below $T_C \approx 20$ K and is also metallic with low-$T$ resistivity at least as low as ∼6.5 m$\Omega$ cm [71]. Gated surfaces reaching resistances as low as ∼10 $\Omega$ are therefore consistent with our EDX and XPS findings. As quantitative

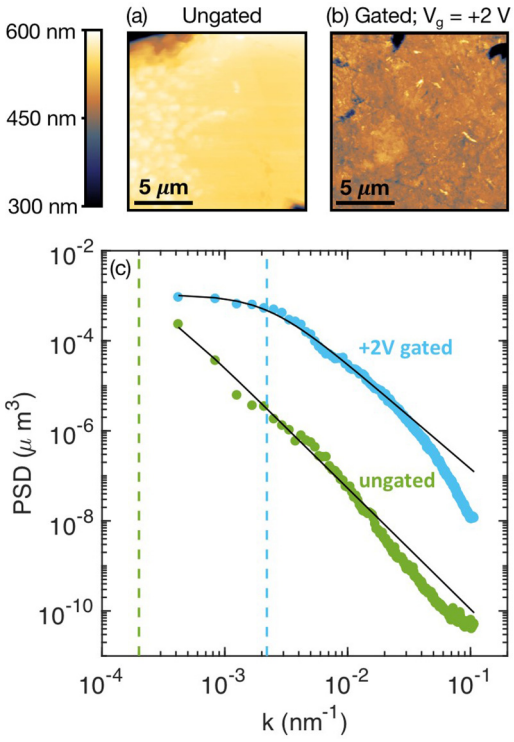


FIG. 4. Contact-mode AFM height images (15 $\mu$m × 15$\mu$m) of (a) ungated and (b) +2.0 V gated $NiS_2$ single-crystal surfaces. The common height scale for the images is displayed on the left; the lower limit for the height scale was set at 300 nm, for better contrast. (c) 1D power spectral density functions for gated (+2.0 V) and ungated samples, as obtained from the AFM height images in (a), (b), using Eqs. (1) and (2). The solid black lines are fits to the $k$-correlation model (see Supplemental Material, Sec. E [57]) used to extract the correlation length. The latter is 4.8(3.6) and 0.45(0.04) $\mu$m from the ungated and gated fits shown. The inverse correlation lengths obtained for the gated and ungated samples are depicted by dashed lines with the respective colors.

support for this, note that a sheet resistance of ∼10 Ω due to a layer hundreds of nm thick corresponds to ∼1 mΩ cm resistivity, easily within reach of mixed phase NiS/$Ni_3S_4$ based on the above literature values.

Moving to surface topography, prior work on gated $La_{1-x}Sr_xCoO_{3-\delta}$ films, for example, revealed that in the high-positive gate-voltage regime where electrochemical mechanisms dominate, gating eventually induces etching, leading to the formation of pits on the film surface [20]. Such electrochemical etching has also been observed in FeSe films on $SrTiO_3$ and MgO substrates [72]. Given the strongly electrochemical nature of the gating uncovered here in $NiS_2$, it therefore seems pertinent to investigate the effects of gating on the topography of the crystal surface. Figures 4(a) and 4(b) thus show contact-mode AFM height images of the surface of an ungated $NiS_2$ crystal and a postgating (+2.0 V) crystal, respectively. The surface topography is indeed distinctly different in the two cases. While approximately micron-scale lateral features are visible in both cases, these occur on different specific scales, at different frequencies, and are associated with different depths. Rich structure is in fact observed in Fig. 4(b) at short lateral length scales, as well as deep pits reminiscent of the etch pits seen in $La_{1-x}Sr_xCoO_{3-\delta}$ [20].

Quantitative analysis of the surface height distribution was performed with the relevant power spectral density (PSD), defined as [73]

$$W(k_x, k_y) = \frac{1}{L^2}\left[\sum_{m=1}^{N}\sum_{n=1}^{N} h_{mn} e^{-2\pi i \Delta L(k_x m + k_y n)} (\Delta L)^2\right]^2, \quad (1)$$

where $L$ is the scan length along both the horizontal and vertical axes, $h_{mn}$ is the profile height at position $(m, n)$, $k_x$ and $k_y$ are the spatial frequencies along the $x$ and $y$ directions, $\Delta L$ is the distance between neighboring sampling points, and $N$ is the total number of sampling points along each direction (with $L = N\Delta L$). One-dimensional (1D) PSDs were then obtained by averaging along the direction perpendicular to the scan direction (i.e., along the $y$ axis in our case):

$$W_1(k) = \frac{1}{L}\sum_{k_y} W(k, k_y). \quad (2)$$

Mathematically, the PSD thus represents the distribution of surface roughness with different associated spatial frequencies, as defined by the inverse wavelength of the topographic features. Thus, higher values of PSD at high frequencies indicate a higher density of low-wavelength features (and vice versa). The 1D PSDs obtained for the ungated and gated crystal surfaces in Figs. 4(a) and 4(b) are shown in Fig. 4(c), where clear differences are apparent. Specifically, the gated PSD (blue) is distinctly shifted to higher spatial frequencies (lower wavelengths), with a knee forming at ∼2.2 $\mu m^{-1}$ (vertical blue dashed line). This indicates a surface with dominant low-wavelength components, the extracted correlation length (from the shown fits [74]; see Supplemental Material, Sec. E [57]) falling by an order of magnitude with respect to the ungated case, from ∼4.8 $\mu$m to ∼450 nm. We believe that this finding is consistent with the above conclusions from spectroscopy. Specifically, conversion of the initial $NiS_2$ single-crystal surface to lower S:Ni phases such as NiS or $Ni_3S_4$ likely occurs with significant lateral inhomogeneity, with multiple phases present, potentially even with associated polycrystallinity. Under such circumstances, low-wavelength structure would be expected in AFM images, as is the case in Fig. 4(b).

Prior to discussing the origins and implications of our findings, we note that substantial additional efforts were devoted to using various forms of XRD to definitively identify the low S:Ni ratio majority phase(s) postgating. This encompassed both lab-based measurements with an area detector and synchrotron-based reciprocal space mapping, as described in the Supplemental Material, Sec. F [57]. Likely hindered by the much larger penetration depth of the x rays in such measurements compared to the thickness of the reduced layer, these attempts were not successful. It is also possible that the low S:Ni ratio phase(s) (and/or oxides and hydroxides) induced by gating are amorphous or weakly crystalline, which would obviously limit the usefulness of XRD.

## IV. DISCUSSION

The above transport, chemical, and structural characterization measurements on electrolyte-gated $NiS_2$ single crystals clearly reveal an electrochemical gating mechanism in $NiS_2$, resulting in substantial decreases in the S:Ni ratio (from 2.0 to close to ∼1.2) over depths of hundreds of nm. These gating-induced changes are both nonvolatile and irreversible, in stark contrast with what is seen in isostructural pyrite $FeS_2$. In this section we provide a hypothesis for these differences, which we believe provides insight into the general issue of understanding electrostatic vs electrochemical response in electrolyte-gated materials.

In the better understood case of electrolyte gating of binary and complex *oxides*, electrochemical response via oxygen vacancy formation/annihilation vs electrostatic accumulation of electrons/holes has been demonstrated to depend strongly on the O vacancy ($V_O$) diffusion coefficient [21,28]. Specifically, recent electrolyte gating investigations of the perovskite oxide $BaSnO_3$, for example, revealed reversible and volatile control of transport properties across a remarkably wide gate-voltage window, which was argued to be a consequence of very low room-temperature $V_O$ diffusivity [28]. In such circumstances, positive $V_g$ may induce $V_O$ formation at the extreme surface of the oxide, but the very slow diffusion prevents proliferation of $V_O$ to greater depths, thus minimizing electrochemical response. At the other extreme, oxides such as $La_{1-x}Sr_xCoO_{3-\delta}$, $SrTiO_3$, $VO_2$, etc., have much higher $V_O$ diffusivity, enabling proliferation of $V_O$ to substantial depths, thereby promoting electrochemical response. In cobaltites, for example, the diffusion length for $V_O$ on the time and temperature scales relevant to typical electrolyte gating experiments can easily exceed 100 nm [21,22].

Extending the above arguments to pyrite-structure $TMS_2$ compounds is revealing. In particular, S and $V_S$ diffusion in $FeS_2$ is notoriously sluggish, the room-temperature-extrapolated S diffusion coefficient of $10^{-37}\,m^2\,s^{-1}$ [53,54] yielding a diffusion length ($\sqrt{Dt}$ where $D$ is the diffusion coefficient and $t$ is time) of $\sim 10^{-17}$ m. In the above picture, this strikingly short length scale would promote an electrostatic electron doping mechanism, exactly as recently deduced from the volatile, highly reversible gate effect [16]. In $NiS_2$ on the other hand, for reasons that are not entirely clear but may be related to cell-volume expansion related to its Mott-insulating character, the S diffusion coefficient has been estimated to be $\sim 10^{-10}\,m^2\,s^{-1}$ at room temperature, i.e., 27 orders of magnitude higher than in $FeS_2$ [52]. This radical difference yields a diffusion length for S vacancies in $NiS_2$ of $\sim 100\,\mu$m, assuming 300 K and 30 min. Critically, this is easily large enough to rationalize the hundreds-of-nm length scales over which gate-induced electrochemistry is found to occur in the present work. As a final note on this point, we remark that while the method used to extract the diffusion coefficient in Ref. [52] is atypical, and should be treated only as an estimate, the enormous difference in $V_S$ diffusivity between $FeS_2$ and $NiS_2$ appears beyond question.

Based on the above findings, the initial phase of the electrolyte gating process in $NiS_2$ likely involves reduction of $NiS_2$ to $NiS_{2-\delta}$, i.e., initial formation of $V_S$. Following this, further S reduction leads to the formation of lower-S-content phases, such as NiS and $Ni_3S_4$, which exist on the bulk equilibrium phase diagram [59], and are known to be metallic in nature. As already noted, the low-S-content Ni-S state formed after gating also appears to exhibit, unsurprisingly for such a strongly electrochemical gating mechanism, significant inhomogeneity, both laterally and depthwise (from XPS data). This high degree of inhomogeneity could contribute to the absence of superconductivity in our transport measurements. Specifically, any superconducting phase generated by electron doping of $NiS_{2-\delta}$ in the early stages of gating would exist at low volume fractions, beneath percolation. We would add that although the primary effect in our gating process is clearly reduction of the S:Ni ratio, it is also possible that $H^+$, formed by electrolysis of water present in the IL [27], could also play some role. This H could be directly inserted, or could lead to formation of hydroxides of Ni, consistent with higher binding energy features observed in our Ni XPS spectra [65,66].

Finally, with an explanation for a strongly nonvolatile, electrochemistry-based, and long-length-scale gating process in hand, we now turn to the observed irreversibility, i.e., the inability to recover $NiS_2$ at negative $V_g$. We believe that the primary issue here is the lack of an atmospheric reservoir of S for resulfidation. In the better understood case of oxides it is widely believed that $H_2O$ present in ILs undergoes electrolysis at finite $V_g$ [3], providing a large reservoir of O for reoxidation of reduced phases. In cobaltites for example, perovskite $SrCoO_3$ can thus be reduced to brownmillerite $SrCoO_{2.5}$ at positive bias, and then reoxidized to $SrCoO_3$ at negative voltage, in a reversible cycle [3,22,27,75,76]. In the case of sulfides, no such S reservoir is obviously available (barring the chemical breakdown of a S-containing component in the electrolyte), which we believe plays the key role in strongly limiting reversibility, as is manifest in Fig. 1. As a secondary factor, it should be noted that the non-$NiS_2$ phases generated by gating likely have much lower S diffusion rates than $NiS_2$. A low S diffusion coefficient is known in NiS, for example, in which case no indiffusion of S was found at 1123 K, under a high S vapor pressure of $10^4$ Pa [77]. This could also then contribute to the observed inability to resulfidize to $NiS_2$ in electrolyte gating at negative gate voltages.

## V. SUMMARY AND CONCLUSIONS

In conclusion, we have revealed a 3D metallic phase in ionic-liquid-gated Mott-insulating $NiS_2$ single crystals, formed at positive gate voltages. The sheet resistance was observed to rapidly decrease with increasing gate voltage. Of highest interest, the electrolyte gate effect is irreversible, nonvolatile, and electrochemical in nature, and proceeds via reduction of the S:Ni ratio to depths of 100s of nm. No superconductivity was detected down to 450 mK in the gated system. These conclusions are supported by electronic transport, spectroscopic, and surface microscopy studies, providing a detailed picture. We explain these features in terms of unusually large sulfur diffusivity in $NiS_2$, which enables nonvolatile reduction over large length scales, as well as the absence of an obvious sulfur reservoir in such gating, which severely limits

reversibility. $NiS_2$ thus illuminates a heretofore unexplored limit of electrolyte gating.

## ACKNOWLEDGMENTS

We thank Liam Thompson for help with electrical contact preparation. This work was supported primarily by the National Science Foundation through the University of Minnesota (UMN) MRSEC under Award No. DMR-2011401. Parts of this work were carried out in the Characterization Facility, UMN, which receives partial support from the NSF through the MRSEC (Award No. DMR-2011401) and the NNCI (Award No. ECCS-2025124) programs.

[1] M. Imada, A. Fujimori, and Y. Tokura, Rev. Mod. Phys. **70**, 1039 (1998).
[2] C. H. Ahn, J.-M. Triscone, and J. Mannhart, Nature (London) **424**, 1015 (2003).
[3] C. Leighton, Nat. Mater. **18**, 13 (2019).
[4] A. M. Goldman, Annu. Rev. Mater. Res. **44**, 45 (2014).
[5] S. Z. Bisri, S. Shimizu, M. Nakano, and Y. Iwasa, Adv. Mater. **29**, 1607054 (2017).
[6] K. Ueno, S. Nakamura, H. Shimotani, H. T. Yuan, N. Kimura, T. Nojima, H. Aoki, Y. Iwasa, and M. Kawasaki, Nat. Nanotechnol. **6**, 408 (2011).
[7] K. Ueno, S. Nakamura, H. Shimotani, A. Ohtomo, N. Kimura, T. Nojima, H. Aoki, Y. Iwasa, and M. Kawasaki, Nat. Mater. **7**, 855 (2008).
[8] K. Ueno, H. Shimotani, Y. Iwasa, and M. Kawasaki, Appl. Phys. Lett. **96**, 252107 (2010).
[9] X. Leng, J. Garcia-Barriocanal, S. Bose, Y. Lee, and A. M. Goldman, Phys. Rev. Lett. **107**, 027001 (2011).
[10] A. T. Bollinger, G. Dubuis, J. Yoon, D. Pavuna, J. Misewich, and I. Božović, Nature (London) **472**, 458 (2011).
[11] M. Nakano, K. Shibuya, D. Okuyama, T. Hatano, S. Ono, M. Kawasaki, Y. Iwasa, and Y. Tokura, Nature (London) **487**, 459 (2012).
[12] J. Jeong, N. Aetukuri, T. Graf, T. D. Schladt, M. G. Samant, and S. S. P. Parkin, Science **339**, 1402 (2013).
[13] S. Asanuma, P. H. Xiang, H. Yamada, H. Sato, I. H. Inoue, H. Akoh, A. Sawa, K. Ueno, H. Shimotani, H. Yuan, M. Kawasaki, and Y. Iwasa, Appl. Phys. Lett. **97**, 142110 (2010).
[14] R. Scherwitzl, P. Zubko, I. G. Lezama, S. Ono, A. F. Morpurgo, G. Catalan, and J. M. Triscone, Adv. Mater. **22**, 5517 (2010).
[15] J. Son, B. Jalan, A. P. Kajdos, L. Balents, S. J. Allen, and S. Stemmer, Appl. Phys. Lett. **99**, 192107 (2011).
[16] J. Walter, B. Voigt, E. Day-Roberts, K. Heltemes, R. M. Fernandes, T. Birol, and C. Leighton, Sci. Adv. **6**, eabb7721 (2020).
[17] J. Walter, T. Charlton, H. Ambaye, M. R. Fitzsimmons, P. P. Orth, R. M. Fernandes, and C. Leighton, Phys. Rev. Materials **2**, 111406(R) (2018).
[18] M. Li, W. Han, X. Jiang, J. Jeong, M. G. Samant, and S. S. P. Parkin, Nano Lett. **13**, 4675 (2013).
[19] T. D. Schladt, T. Graf, N. B. Aetukuri, M. Li, A. Fantini, X. Jiang, M. G. Samant, and S. S. P. Parkin, ACS Nano **7**, 8074 (2013).
[20] J. Walter, H. Wang, B. Luo, C. D. Frisbie, and C. Leighton, ACS Nano **10**, 7799 (2016).
[21] J. Walter, G. Yu, B. Yu, A. Grutter, B. Kirby, J. Borchers, Z. Zhang, H. Zhou, T. Birol, M. Greven, and C. Leighton, Phys. Rev. Materials **1**, 071403(R) (2017).
[22] V. Chaturvedi, W. M. Postiglione, R. D. Chakraborty, B. Yu, W. Tabiś, S. Hameed, N. Biniskos, A. Jacobson, Z. Zhang, H. Zhou, M. Greven, V. E. Ferry, and C. Leighton, ACS Appl. Mater. Interfaces **13**, 51205 (2021).
[23] C. Song, B. Cui, F. Li, X. Zhou, and F. Pan, Prog. Mater. Sci. **87**, 33 (2017).
[24] K. Shibuya and A. Sawa, Adv. Electron. Mater. **2**, 1500131 (2016).
[25] X. Leng, J. Pereiro, J. Strle, G. Dubuis, A. T. Bollinger, A. Gozar, J. Wu, N. Litombe, C. Panagopoulos, D. Pavuna, and I. Božović, npj Quantum Mater. **2**, 35 (2017).
[26] H. Ji, J. Wei, and D. Natelson, Nano Lett. **12**, 2988 (2012).
[27] N. Lu, P. Zhang, Q. Zhang, R. Qiao, Q. He, H.-B. Li, H.-B. Li, Y. Wang, J. Guo, D. Zhang, Z. Duan, Z. Li, M. Wang, S. Yang, M. Yan, E. Arenholz, S. Zhou, W. Yang, L. Gu, C.-W. Nan, J. Wu, Y. Tokura, and P. Yu, Nature (London) **546**, 124 (2017).
[28] H. Wang, J. Walter, K. Ganguly, B. Yu, G. Yu, Z. Zhang, H. Zhou, H. Fu, M. Greven, and C. Leighton, Phys. Rev. Materials **3**, 075001 (2019).
[29] S. Ogawa, J. Appl. Phys. **50**, 2308 (1979).
[30] A. Ennaoui, S. Fiechter, Ch. Pettenkofer, N. Alonso-Vante, K. Büker, M. Bronold, Ch. Höpfner, and H. Tributsch, Sol. Energy Mater. Sol. Cells **29**, 289 (1993).
[31] H. S. Jarrett, W. H. Cloud, R. J. Bouchard, S. R. Butler, C. G. Frederick, and J. L. Gillson, Phys. Rev. Lett. **21**, 617 (1968).
[32] K. Kikuchi, J. Phys. Soc. Jpn. **47**, 484 (1979).
[33] T. Thio, J. W. Bennett, and T. R. Thurston, Phys. Rev. B **52**, 3555 (1995).
[34] T. Thio and J. W. Bennett, Phys. Rev. B **50**, 10574 (1994).
[35] P. G. Niklowitz, P. L. Alireza, M. J. Steiner, G. G. Lonzarich, D. Braithwaite, G. Knebel, J. Flouquet, and J. A. Wilson, Phys. Rev. B **77**, 115135 (2008).
[36] J. M. Hastings and L. M. Corliss, Phys. Rev. B **14**, 1995 (1976).
[37] K. Persson, G. Ceder, and D. Morgan, Phys. Rev. B **73**, 115201 (2006).
[38] C. Leighton, M. Manno, A. Cady, J. W. Freeland, L. Wang, K. Umemoto, R. M. Wentzcovitch, T. Y. Chen, C. L. Chien, P. L. Kuhns, M. J. R. Hoch, A. P. Reyes, W. G. Moulton, E. D. Dahlberg, J. Checkelsky, and J. Eckert, J. Phys.: Condens. Matter **19**, 315219 (2007).
[39] N. B. M. Schröter, I. Robredo, S. Klemenz, R. J. Kirby, J. A. Krieger, D. Pei, T. Yu, S. Stolz, T. Schmitt, P. Dudin, T. K. Kim, C. Cacho, A. Schnyder, A. Bergara, V. N. Strocov, F. de Juan, M. G. Vergniory, and L. M. Schoop, Sci. Adv. **6**, eabd5000 (2020).
[40] L. Wang, T. Y. Chen, C. L. Chien, J. G. Checkelsky, J. C. Eckert, E. D. Dahlberg, K. Umemoto, R. M. Wentzcovitch, and C. Leighton, Phys. Rev. B **73**, 144402 (2006).
[41] L. Wang, K. Umemoto, R. M. Wentzcovitch, T. Y. Chen, C. L. Chien, J. G. Checkelsky, J. C. Eckert, E. D. Dahlberg, and C. Leighton, Phys. Rev. Lett. **94**, 056602 (2005).

[42] S. Ogawa, S. Waki, and T. Teranishi, Int. J. Magn. **5**, 349 (1974).
[43] J. Walter, X. Zhang, B. Voigt, R. Hool, M. Manno, F. Mork, E. S. Aydil, and C. Leighton, Phys. Rev. Materials **1**, 065403 (2017).
[44] M. Limpinsel, N. Farhi, N. Berry, J. Lindemuth, C. L. Perkins, Q. Lin, and M. Law, Energy Environ. Sci. **7**, 1974 (2014).
[45] M. Cabán-Acevedo, N. S. Kaiser, C. R. English, D. Liang, B. J. Thompson, H. Chen, K. J. Czech, J. C. Wright, R. J. Hamers, and S. Jin, J. Am. Chem. Soc. **136**, 17163 (2014).
[46] D. Liang, M. Cabán-Acevedo, N. S. Kaiser, and S. Jin, Nano Lett. **14**, 6754 (2014).
[47] S. El-Khatib, B. Voigt, B. Das, A. Stahl, W. Moore, M. Maiti, and C. Leighton, Phys. Rev. Materials **5**, 115003 (2021).
[48] D. D. Sarma, S. R. Krishnakumar, E. Weschke, C. Schüßler-Langeheine, C. Mazumdar, L. Kilian, G. Kaindl, K. Mamiya, S.-I. Fujimori, A. Fujimori, and T. Miyadai, Phys. Rev. B **67**, 155112 (2003).
[49] S. Friedemann, H. Chang, M. B. Gamza, P. Reiss, X. Chen, P. Alireza, W. A. Coniglio, D. Graf, S. Tozer, and F. M. Grosche, Sci. Rep. **6**, 25335 (2016).
[50] J. M. Honig and J. Spalek, Chem. Mater. **10**, 2910 (1998).
[51] H. S. Jarrett, R. J. Bouchard, J. L. Gillson, G. A. Jones, S. M. Marcus, and J. F. Weiher, Mater. Res. Bull. **8**, 877 (1973).
[52] C. Clark and S. Friedemann, J. Magn. Magn. Mater. **400**, 56 (2016).
[53] E. B. Watson, D. J. Cherniak, and E. A. Frank, Geochim. Cosmochim. Acta **73**, 4792 (2009).
[54] Y. N. Zhang, M. Law, and R. Q. Wu, J. Phys. Chem. C **119**, 24859 (2015).
[55] http://gwyddion.net/.
[56] D. Nečas and P. Klapetek, Cent. Eur. J. Phys. **10**, 181 (2012).
[57] See Supplemental Material at http://link.aps.org/supplemental/10.1103/PhysRevMaterials.6.064601 for additional gating data on $NiS_2$ single crystals with pristine top surfaces and polished bottom surfaces, gating data on double-side-polished $NiS_2$ single crystals, depth-profile and lateral variability of XPS of gated and ungated samples, additional XPS data on gated and ungated samples, quantitative analysis of PSD from AFM images, and XRD data.
[58] https://www.gel.usherbrooke.ca/casino/.
[59] H. Okamoto, J. Phase Equilibria Diffus. **30**, 123 (2009).
[60] P. Luo, H. Zhang, L. Liu, Y. Zhang, J. Deng, C. Xu, N. Hu, and Y. Wang, ACS Appl. Mater. Interfaces **9**, 2500 (2017).
[61] X. Zhang, T. Scott, T. Socha, D. Nielson, M. Manno, M. Johnson, Y. Yan, Y. Losovyj, P. Dowben, E. S. Aydil, and C. Leighton, ACS Appl. Mater. Interfaces **7**, 14130 (2015).
[62] C. Xu, B. Sun, T. Gustafsson, K. Edström, D. Brandell, and M. Hahlin, J. Mater. Chem. A **2**, 7256 (2014).
[63] G. Greczynski and L. Hultman, Appl. Surf. Sci. **542**, 148599 (2021).
[64] J. Deng, Q. Gong, H. Ye, K. Feng, J. Zhou, C. Zha, J. Wu, J. Chen, J. Zhong, and Y. Li, ACS Nano **12**, 1829 (2018).
[65] A. P. Grosvenor, M. C. Biesinger, R. St. C. Smart, and N. S. McIntyre, Surf. Sci. **600**, 1771 (2006).
[66] M. C. Biesinger, B. O. Payne, L. W. M. Lau, A. Gerson, and R. St. C. Smart, Surf. Interface Anal. **41**, 324 (2009).
[67] J. T. Sparks and T. Komoto, Rev. Mod. Phys. **40**, 752 (1968).
[68] P. Chen and Y. W. Du, Europhys. Lett. **53**, 360 (2001).
[69] L. J. Pauwels and G. Maervoet, Bull. Soc. Chim. Belges **80**, 501 (1971).
[70] L. J. Pauwels and G. Maervoet, Bull. Soc. Chim. Belges **81**, 385 (1972).
[71] A. Manthiram and Y. U. Jeong, J. Solid State Chem. **147**, 679 (1999).
[72] J. Shiogai, Y. Ito, T. Mitsuhashi, T. Nojima, and A. Tsukazaki, Nat. Phys. **12**, 42 (2016).
[73] S. J. Fang, S. Haplepete, W. Chen, C. R. Helms, and H. Edwards, J. Appl. Phys. **82**, 5891 (1997).
[74] A. A. Ponomareva, V. A. Moshnikov, and G. Suchaneck, IOP Conf. Ser.: Mater. Sci. Eng. **47**, 012052 (2013).
[75] Q. Lu, S. Huberman, H. Zhang, Q. Song, J. Wang, G. Vardar, A. Hunt, I. Waluyo, G. Chen, and B. Yildiz, Nat. Mater. **19**, 655 (2020).
[76] S. Ning, Q. Zhang, C. Occhialini, R. Comin, X. Zhong, and C. A. Ross, ACS Nano **14**, 8949 (2020).
[77] Z. Grzesik, A. Poczekajło, and S. Mrowec, Defect Diffus. Forum **323**, 315 (2012).